Materials Advances

ROYAL SOCIETY OF CHEMISTRY

PAPER

View Article Online
View Journal | View Issue

Cite this: *Mater. Adv.*, 2025, 6, 977

Comparative analysis of monomeric *vs.* dimeric salen fluorescent probes: transition from a turn-on to ratiometric response towards nerve gas agents in organic to aqueous media†

Sourav Mondal and Nilanjan Dey *

Nerve agents are among the most hazardous chemical warfare agents, requiring easy detection and prompt remediation. To this end, we synthesized two fluorescent salen molecules, **P-1** (dimeric) and **P-2** (monomeric), for the detection of diethyl chlorophosphate (DClP), a mimic of sarin and soman, in an aqueous medium. **P-1** exhibited a stronger fluorescence response (~22.0-fold) towards DClP than **P-2** (~1.1-fold). This superior performance of **P-1** could be attributed to its dimeric structure, difference in aggregation, and photophysical properties. The mechanistic studies revealed that DClP-mediated phosphorylation of the hydroxy groups led to changes in the keto–enol equilibrium and aggregation state of compound **P-1**. Unlike in an aqueous medium, **P-1** in DMSO medium displayed a turn-on fluorescence response towards DClP. The minimum detectable limit for DClP resulted in ~5.0 ppb in an aqueous medium. **P-1** was also effective in detecting DClP in soil samples, with a detection limit of ~15.0 ppb, a recovery of 95.4–97.8%, and a relative standard deviation (RSD) within 2–3%, demonstrating the reliability and robustness of the present method. Finally, chemically modified dye coated paper strips were developed for rapid and on site detection of release of nerve gas vapour beyond permissible limit.

Received 9th October 2024,
Accepted 4th December 2024

DOI: 10.1039/d4ma01016g

rsc.li/materials-advances

1. Introduction

Nerve agents, potent organophosphorus compounds, inhibit acetylcholinesterase (AChE), causing acetylcholine (ACh) buildup and continuous nerve activation. This leads to paralysis of respiratory muscles and high exposure can result in death.[1–6] Hence, its early and quick detection was necessary. However, there are numerous nerve agents with lethal effects that share structural similarities, making their detection and differentiation challenging. Despite similar emergency response protocols for all nerve agents, differences in toxicity and evidence that some antidotes are ineffective against certain agents highlight the importance of distinguishing between specific compounds within this toxic chemical family.[7] For example, although tabun and soman have similar toxicity, they require different antidotes and medical treatments.[8] Hence, developing a sensor that can detect and discriminate nerve gas mimics is necessary.

Detecting nerve gas mimics in water is critical because water enhances sensor sensitivity and stabilizes the phosphonate product. As a polar solvent, water facilitates the formation of hydrolytically stable complexes with mimics such as diethyl chlorophosphate (DClP) or diethyl cyanophosphate (DCNP), which exhibit lower solubility and stability in organic solvents.[9] Additionally, water provides a buffered environment that minimizes the effect of the microenvironment compared to organic solvents. Consequently, water-phase detection of nerve gas mimics is advantageous for monitoring their presence in environmental samples, including water and soil, as contamination of soil and water by chemical warfare agents (CWAs) poses serious risks to both civilian and military populations, potentially causing severe health problems or fatalities.[10]

Various methods like enzyme assays, electrochemistry, and interferometry are used to detect nerve agents, but they often struggle with specificity, complexity, and real-time monitoring. Optical sensors, such as colorimetric and fluorometric, offer a simpler, more portable, and potentially more reliable alternative.[11–13] Many fluorescent sensors have been developed for detecting nerve gas mimics like DClP or DCNP (diethyl cyanophosphate), but most of them lack selectivity for these structurally similar toxins and struggle to detect them in aqueous environments. This limitation reduces their effectiveness for environmental applications.[14–17]

Fluorescent salen-based derivatives having both hydroxy and imine groups as binding sites showed ESIPT (excited-state intra-molecular proton transfer) properties where the hydroxyl

Department of Chemistry, Birla Institute of Technology and Science Pilani, Hyderabad Secunderabad, Telangana 500078, India.
E-mail: nilanjandey.iisc@gmail.com, nilanjan@hyderabad.bits-pilani.ac.in

† Electronic supplementary information (ESI) available. See DOI: https://doi.org/10.1039/d4ma01016g

hydrogen in the salen ligand transfers to the imine nitrogen. These systems also display strong aggregation-induced emissions (AIE) in water.[18] These properties make this molecule ideal as a sensing material by changing either the aggregation or keto–enol tautomerization. Again, a salen based system can show a ratiometric response upon interaction with the analyte.[19] These ratiometric fluorescent sensors can minimize interference from unrelated factors due to their inherent self-calibration capabilities. This feature enhances their sensitivity and provides clearer visual detection, making them more effective for qualitative and quantitative analysis.[20] Recently, salen based fluorescent probes were largely used for the ratiometric sensing of cations, anions and small molecule.[21–27] Hence, a ratiometric salen-based probe can be used to detect and differentiate organophosphate-based nerve gas mimics like DClP or DCNP.

Hence, we synthesized two fluorescent salen-based ESIPT active probes **P-1** and **P-2** (Fig. 1a) to detect and discriminate nerve gas mimics DClP and DCNP in aqueous media. Here **P-1** is dimeric whereas **P-2** is a monomeric salen derivative and depending on the structure their ESIPT and aggregation properties were altered. Both the compounds showed a change in fluorescence intensity with the gradual addition of DClP. **P-1** exhibited a stronger fluorescence response (~22.0-fold) towards DClP than **P-2** (~1.1-fold). The superior performance of **P-1** compared to **P-2** is attributed to its greater number of phosphorylation binding sites, higher degree of aggregation in solution, and increased enol emission. The **P-1** compound showed a ratiometric change in fluorescence intensity on the gradual addition of DClP or DCNP in an aqueous medium. However, the extent of change was greater in the case of DClP (~7.0-fold) compared to DCNP (~2.0-fold) indicating that the sensor was highly selective for DClP. The mechanistic investigation (such as using FTIR, NMR, and Mass) suggested that phosphorylation of the hydroxyl group along with a change in aggregation led to an alteration of the keto–enol equilibrium and was responsible for the sensing of DClP (Fig. 1c). Again, a detailed mechanistic study was carried out to understand the effect of solvents (organic and aqueous), temperature, and time of interaction between the probe and analyte. The compound **P-1** exhibited a change in the ratiometric response to DClP in an aqueous medium while showing only turn-on sensing in DMSO. This may be attributed to the alteration in the keto–enol equilibrium and the extent of aggregation of **P-1** in the two solvents. Specifically, the **P-1** compound exhibited a ~22.0-fold increase in fluorescence intensity at 450 nm in water upon the addition of DClP whereas in DMSO, the fluorescence intensity increased by ~5.2-fold at 465 nm. Then the **P-1** compound was employed to detect DClP in the spiked soil solution. Finally, sample-coated paper strips of **P-1** were prepared for easy on-location detection of nerve gases in the vapor phase.

2. Experimental section

2.1 Materials and methods

All the reagents and spectroscopic grade solvents were purchased from the respective vendors and suppliers such as Merck, Avra, Alfa Acer, *etc.*, and used without further purification. The buffer solution was prepared following the standard literature procedure. The UV-Vis measurements were carried out using a Jasco 650 spectrophotometer, whereas the fluorescence spectra were recorded on a Shimadzu model RF-6000

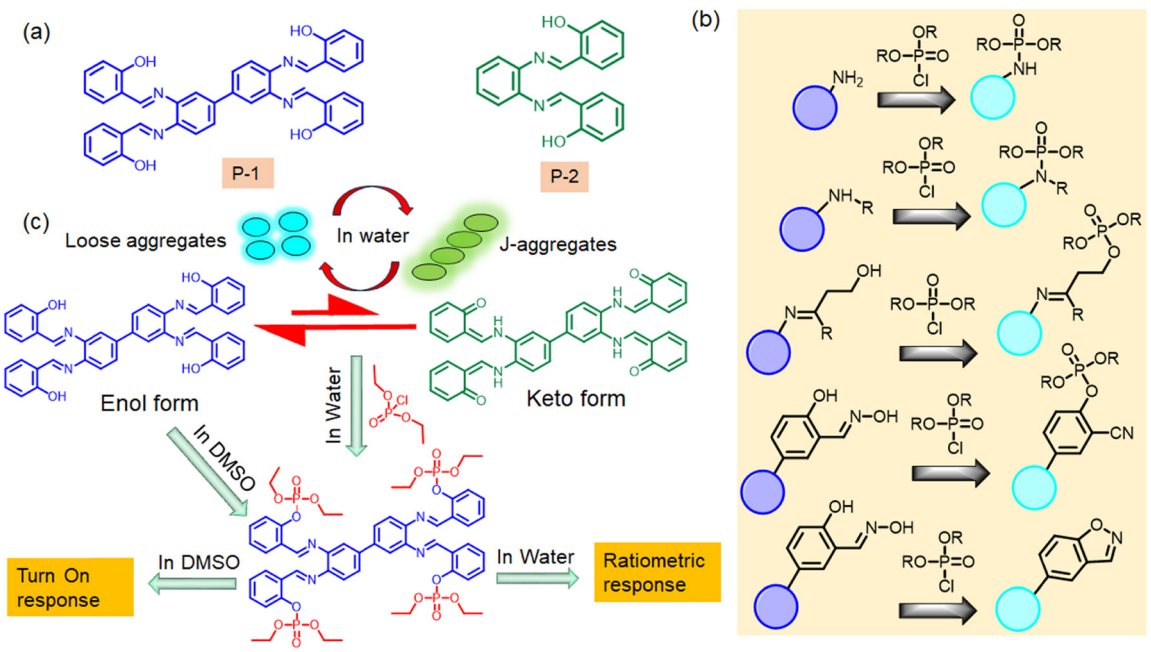

Fig. 1 (a) Structure of the compounds **P-1** and **P-2**. (b) The functional groups already reported for nerve gas sensing. (c) Schematic represents the sensing of DClP by the **P-1** compound in water and DMSO.

spectrophotometer. The slit-width was kept at 5 nm throughout the experiment. Fluorescence lifetime measurement was performed using a time-correlated single photon counting fluorimeter (TCSPC by Horiba). FTIR spectra were recorded on the PerkinElmer FTIR Spectrum BX instrument by making a KBr pellet. FESEM images were obtained using a Quanta 200 SEM instrument (operated at 15 kV) by drop casting the sample on the silicon wafer and then dried in a hot-air oven at 70 °C. ^{1}H and ^{31}P NMR spectra were recorded with a Bruker Advance DRX 400 spectrometer operating at 400 MHz. Particle size analysis was carried out in an aqueous solution using an Anton Paar lite sizer DLS instrument.

2.2 Design and synthesis of the probe molecules

Fluorescent sensors for the detection of nerve gases mostly contain either primary or secondary amine, hydroxyl, or oxime functional groups in their backbone which may be phosphorylated or protonated and, in some cases, formed hydrogen bonding upon the addition of nerve gases giving a fluorogenic response (Fig. 1b). In the development of various fluorescent sensors or probes, ratio-metric fluorescent probes have garnered significant interest. These probes measure the ratio of emission intensities at two distinct wavelengths, offering a built-in correction for background effects and enhancing the dynamic range of fluorescence measurements.[28] The ESIPT-based fluorescent probes showed a ratiometric change in fluorescence intensity upon interaction with the analyte. Again, the large fluorescence Stokes shift and ultrafast reaction rate of the ESIPT-based probes were useful for their potential applications in optical sensing.[29] A molecule containing the hydroxy group can show ESIPT properties where ring hydrogen can take part in the tautomerization losing aromaticity of the ring.[30] On the other hand, in salen-based derivatives, the presence of the imine bond imparts dynamic covalent character, enhancing their ESIPT properties by involving in keto–enol tautomerization.

This dynamic nature provides molecular flexibility, reversibility, tunability, and environmental responsiveness, which contribute to improving ESIPT efficiency. These features allow for the optimization of the molecular structure and aggregation behavior, leading to improved ESIPT efficiency and it can be useful for sensing applications.[31] Again, the difference in the molecular structure of the probe can alter the aggregation and keto–enol tautomerization.

Hence, we designed dimeric (**P-1**) and monomeric (**P-2**) salen-based derivatives to explore their interactions with a nerve agent mimic DClP. These derivatives were synthesized by reacting 3,3′-diaminobenzidine or *o*-phenylenediamine with salicylaldehyde in an ethanolic medium under reflux. The resulting precipitates were filtered to obtain the pure products labeled as **P-1** and **P-2,** respectively. Detailed synthetic procedures are provided in the ESI† of the manuscript.

The synthesized compounds were thoroughly characterized by ^{1}H-NMR and FTIR spectroscopy. Both **P-1** and **P-2** compounds showed characteristic peaks at δ = 8.6 ppm (Fig. S1 and S2, ESI†) owing to the proton associated with the azomethine group in their NMR spectra and no peak for the residual aldehydic proton was observed. In the FTIR spectra of **P-1**, a characteristic peak was observed at 1614 cm^{-1} (Fig. S3, ESI†) which was attributed to the imine bond whereas in the case of **P-2**, a distinct peak at 1617 cm^{-1} was observed for the imine bond (Fig. S4, ESI†).

3. Results and discussion

3.1 Photophysical and aggregation properties of the probes

ESIPT and aggregation properties of these two probes were thoroughly investigated using spectroscopic investigations. Initially, the emission spectra of the probes **P-1** and **P-2** were recorded in different organic solvents including water to understand the effect of solvatochromism on the keto–enol equilibrium.[32] **P-1** showed one emission band in acetonitrile with a smaller Stokes shift at 460 nm indicating the enol emission (Fig. 2a) whereas the compound **P-2** showed two emission bands in acetonitrile at 450 and 530 nm, with a smaller stoke shift for the enol band and a higher stoke shift for the keto band (Fig. 2b). For the compound **P-1** in THF to methanol, we did not observe any additional peak in the higher wavelength region which indicated that despite the change in polarity, the enol form remained in the predominant tautomer form in all the solvents. However, upon increasing polarity, we observed a blue shift in the emission maxima which may be attributed to the hydrogen bonding interactions with the solvent molecules with the enol form.[33] However, in water, the compound **P-1** exhibited red-shifted emission peaks at 550 nm due to the formation of aggregated species (Fig. 2a). In contrast, for compound **P-2**, we observed that upon changing the solvent from acetonitrile (E_{Keto}/E_{enol} = 0.72) to MeOH and THF (E_{Keto}/E_{enol} = 0.18), the emission band belonging to the enol form enhanced, which indicated that the tautomeric equilibrium shifted more towards the enol form in THF and MeOH. In the case of water, the **P-2** compound showed an intense red-shifted emission band at 540 nm due to aggregate formation, along with keto emission and the E_{keto}/E_{enol} ratio sharply increased by 9.5 (Fig. 2b).

To better understand how water affects the aggregation and keto–enol equilibrium, we conducted an experiment where we measured the emission spectra of two probes (**P-1** and **P-2**) in a DMSO medium with varying percentages of the water content (Fig. 2c and d).[34] For **P-1**, we observed that when up to 25% water was added, the emission spectra at 465 nm became blue-shifted, indicating hydrogen bonding interactions with the solvent molecule in the enol form. At 50% water content, a new red-shifted aggregated band appeared at 547 nm, indicating aggregation in water.[35] At 75% water, the intensity of enol emission decreased significantly and the aggregated band shifted slightly to 550 nm. At 100% water, the enol emission intensity decreased further, and the compound showed mostly aggregated emission (Fig. 2c). Again, in the case of **P-2**, two emission bands were observed at 437 nm and 525 nm in DMSO. The band at 437 nm corresponds to the enol emission, while the band at 525 nm corresponds to the keto emission. When the water content is up to 25%, the enol emission remains unchanged, but the keto emission decreases. When the water content is increased to 50%, the

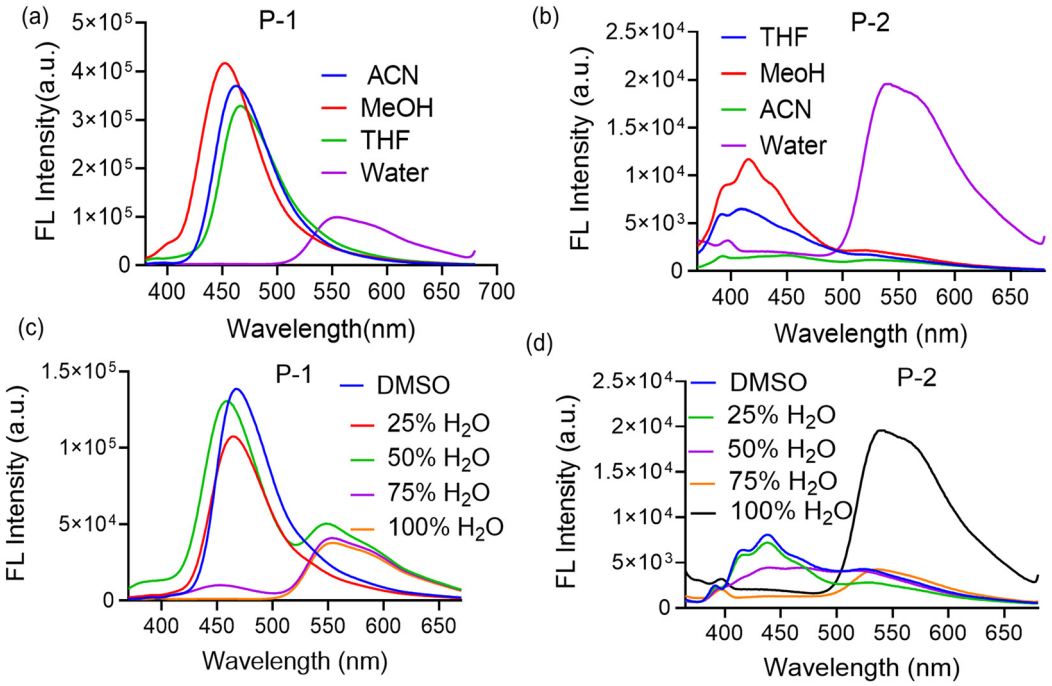

Fig. 2 (a) Emission spectra of **P-1** (10 μM) in different solvents (λ_{ex} = 350 nm). (b) Emission spectra of **P-2** (10 μM) in different solvents (λ_{ex} = 350 nm). (c) Emission spectra of **P-1** (10 μM) under varying water content percentages in DMSO medium (λ_{ex} = 350 nm). (d) Emission spectra of **P-2** (10 μM) under varying water content percentages in DMSO medium (λ_{ex} = 350 nm).

abundance of enol and keto emission becomes equal. At 75% water content, the enol emission further decreases, and the keto emission band shifts to 537 nm, possibly due to aggregation of **P-2** in water. Finally, at 100% water content, the fluorescence intensity of the band at 537 nm sharply increases, indicating aggregation of **P-2** in water along with keto emission (Fig. 2d).

Again, the absorption spectra of both the compounds were recorded in water, **P-1** showed a broad, red-shifted absorption maximum at ~355 nm, whereas **P-2** showed an absorption maximum at ~340 nm (Fig. 3a). This red-shifted absorption spectra of **P-1** may be attributed to its greater hydrogen bonding ability and a higher extent of aggregation in water compared to **P-2**.[36]

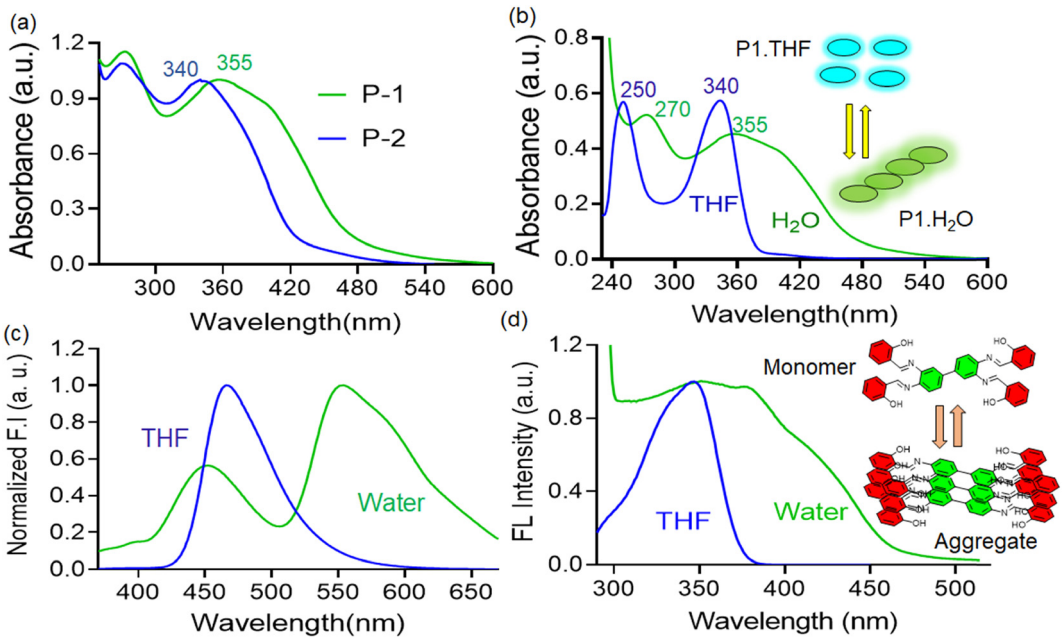

Fig. 3 (a) UV-visible spectra of **P-1** and **P-2** (10 μM) in water. (b) UV-visible spectra of **P-1** (10 μM) in water and THF. (c) Emission spectra of **P-1** (10 μM) in water and THF (λ_{ex} = 350 nm). (d) Fluorescence excitation spectra of **P-1** (10 μM) in water and THF.

3.2 Effect of the microenvironment on self-assembly of probe molecules

To understand the nature of aggregation formed in water we recorded and compared the absorption and emission spectra of the compound **P-1** in water and THF. In water, the **P-1** compound showed dual absorption maxima at ~270 and ~355 nm (Fig. 3b), which can be attributed to the enol and keto isomers, respectively.[32] In contrast, in THF **P-1** exhibited absorption maxima at ~250 and 340 nm (Fig. 3b). The broad and red-shifted absorption maximum at 355 nm in water compared to THF indicated aggregation of the **P-1** compound in water due to stronger hydrogen bonding interactions.[37] Similarly, the emission spectra of **P-1** were recorded in both solvents. In water, **P-1** exhibited dual emission maxima at ~450 and 550 nm (Fig. 3c), while in THF, it showed a single emission maximum at ~465 nm (Fig. 3c). The red-shifted aggregated emission at 550 nm in water may be attributed to an increase in π–π stacking interactions, facilitated by hydrogen bonding interactions, and the formed J-aggregates.[38] The broad and red-shifted excitation spectra of compound **P-1** in water (at 550 nm), compared to THF (at 465 nm) (Fig. 3d), also indicated aggregation of the compound in water. The excitation spectra of compound **P-1** alone in water were recorded at two emission maxima (450 and 550 nm). The broad and red-shifted excitation spectra at 550 nm compared to 450 nm suggest that this band arises due to the formation of aggregated species (Fig. 4a).

Further fluorescence lifetime measurements of the probe **P-1** were carried out in water and THF. The **P-1** compound showed a longer average lifetime (~2.5 ns) in THF compared to water (~0.15 ns) (Fig. 4b). In THF, **P-1** mostly exists in the enol form. The lifetime is mostly attributed to the enol emission. In contrast, the **P-1** compound undergoes more π–π stacking interactions in water, forming J-aggregates, and resulting in a lower fluorescence lifetime in water.[39,40] There was not much effect of the pH (4–8) on the fluorogenic response of the **P-1** probe, the population of the enol and aggregated band remained almost unchanged (Fig. S5, ESI†). To understand the effect of temperature on the aggregation band of **P-1**, the fluorogenic response of **P-1** was recorded at different temperatures (Fig. S6, ESI†). As the temperature increased from 20 °C to 90 °C, there was a sharp decrease in fluorescence intensity at the ~550 nm band and a slight increase in fluorescence intensity at the ~450 nm band. This behavior may be attributed to the decrease in the extent of restricted intermolecular rotation, which led to the destruction of the aggregated structure.[41] We also recorded the absorption spectra of the compound **P-1** in water at different time intervals, which showed almost no change in the absorbance value at the 350 nm band, also indicating the stability of the imine bond present in **P-1** (Fig. S7, ESI†).

Then particle size measurement was carried out to understand the morphology of both compounds in an aqueous medium. The **P-1** compound showed a hydrodynamic diameter of ~190 ± 10 nm (Fig. 4c). In contrast, the **P-2** compound showed ~150 ± 10 nm (Fig. 4d). Again, FESEM images of the **P-1** compound showed a bigger spherical morphology compared to **P-2** which also supported that the **P-1** compound more aggregated than **P-2** in water. Furthermore, WAXS data were compared to understand the nature of crystallinity of the two compounds in the solid state. The **P-1** compound was amorphous, whereas the **P-2** compound was crystalline (Fig. 4e).

3.3 Dual-mode, ratiometric response towards nerve gas agents

The UV-visible absorption spectra were recorded during titrations of the **P-1** with the addition of DClP or DCNP in aqueous

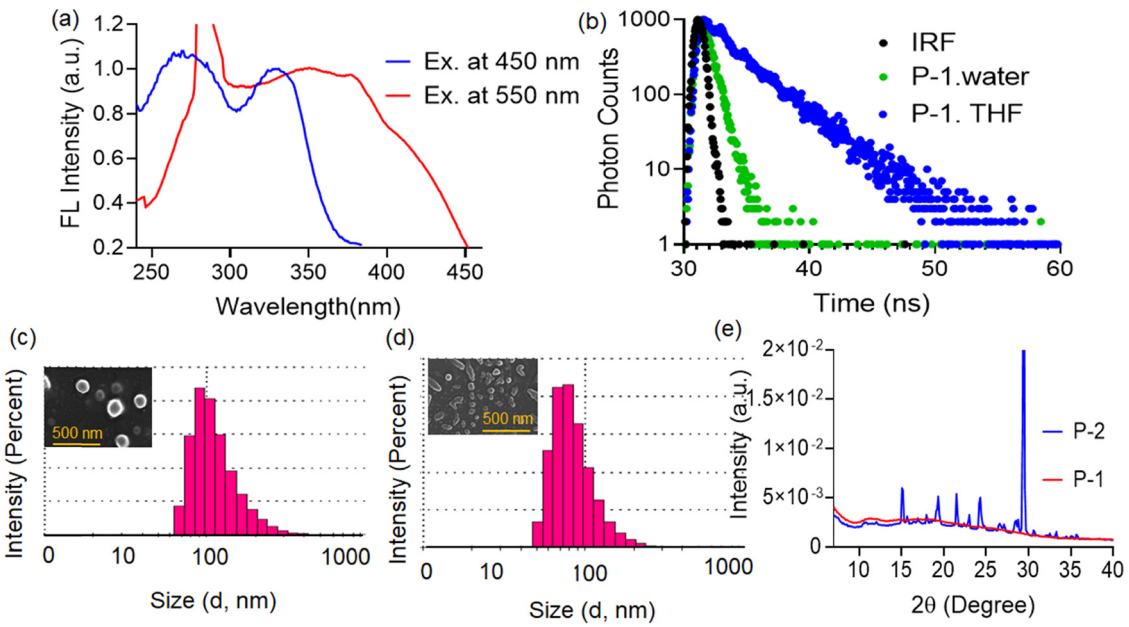

Fig. 4 (a) Fluorescence excitation spectra of the compound **P-1** (10 μM) at 450 and 550 nm in an aqueous medium. (b) Fluorescence lifetime of **P-1** (10 μM) in water and THF (at 460 nm and 550 nm) (λ_{ex} = 350 nm). (c) DLS and FESEM (onset) images of **P-1**. (d) DLS and FESEM (onset) images of **P-2**. (e) WAXS data of **P-1** and **P-2**.

media. In both cases upon the addition of DClP or DCNP, the absorption maxima at 355 nm gradually decreased and it became broad and blue shifted to ~344 nm and the yellow colour of the solution became lighter (Fig. 5a and b). This hypochromic shift in absorbance may be attributed to the incorporation of a strong electrophilic phosphonate group, which in turn terminates the n-π* transitions.[42] Additionally, the blue shift in the absorption spectra upon adding DClP or DCNP to the solution of **P-1** may be attributed to the formation of a phosphorylated product.[43] The broad tailing observed in the absorbance spectra with the addition of DCNP or DClP may be due to the formation of larger aggregated species.[44]

Again, fluorescence titration of **P-1** was recorded with the addition of DCNP or DClP in aqueous media (Fig. 5c and d). The **P-1** compound showed two emission maxima at ~450 and 550 nm. The red-shifted band at 550 nm for aggregated emission gradually decreases, and the blue-shifted band at 450 nm for enol emission gradually increases with the addition of DClP or DCNP. But the extent of ratio-metric change was significant in the case of DClP (~7.0 fold) compared to DCNP (~2.0 fold) (Fig. S8, ESI†). This result indicated that probe **P-1** was more sensitive towards DClP than DCNP. The greater sensitivity to DClP over DCNP may be due to the greater leaving aptitude of the chlorine group in DClP compared to the leaving aptitude of the cyanide group in DCNP upon phosphorylation.[5] The enhancement in the fluorescence intensity of the emission band at 450 nm was attributed to more enol emission due to the conversion of the –OH group into a phosphoester.[45] Again, the quenching of the aggregated band at 550 nm may be attributed to the destruction of the aggregated structure with the addition of DClP. No other analytes, except HCl, showed a similar response to **P-1** under the same conditions (Fig. 6a). The minimum detectable range of **P-1** for DClP was as low as ~5.0 ppb (see the ESI†).

3.4 Mechanistic investigation with nerve gas agents

Several spectroscopic investigations were conducted to explore the sensing mechanism of DClP using probe **P-1**. Initially, fluorescence titration of **P-1** with DClP was carried out at two different temperatures (25 °C and 50 °C) to understand the impact of temperature on sensing (Fig. 6b). At an elevated temperature of 50 °C, the change in fluorescence intensity (F_{450}/F_{550}) was more compared to that at room temperature (25 °C), which may be attributed to the fact that at the higher temperature, the rate of phosphorylation of the phenolic-OH will be more compared to that at room temperature as the phosphorylation reaction was favored at a higher temperature.[46] At higher temperatures, J-aggregation of the probe is disrupted, increasing monomeric emission.[47] This also contributed to the enhancement of fluorescence intensity upon DClP addition at higher temperatures.

Again, the absorption spectra of the **P-1** compound were recorded with and without DClP and HCl, (Fig. 6c) but there was a marginal change in the absorption spectra of **P-1** upon the addition of HCl compared to DClP which indicated less interference of HCl in the DClP sensing. Furthermore, the excitation spectra of **P-1** were recorded with and without DClP and the excitation spectra of **P-1** were red-shifted and broad compared to those of the adduct **P-1@DClP** which indicated the possibility of breaking of J-aggregates as well as an increase in enol emission (Fig. 6d).[48]

For further investigation, the FTIR spectra of **P-1** were recorded both with and without DClP (Fig. 7a). DClP exhibited characteristic peaks at 3230 cm^{-1} for –OH groups (from moisture) and at 2988 cm^{-1} for methylene groups.[49] Upon interaction with **P-1**,

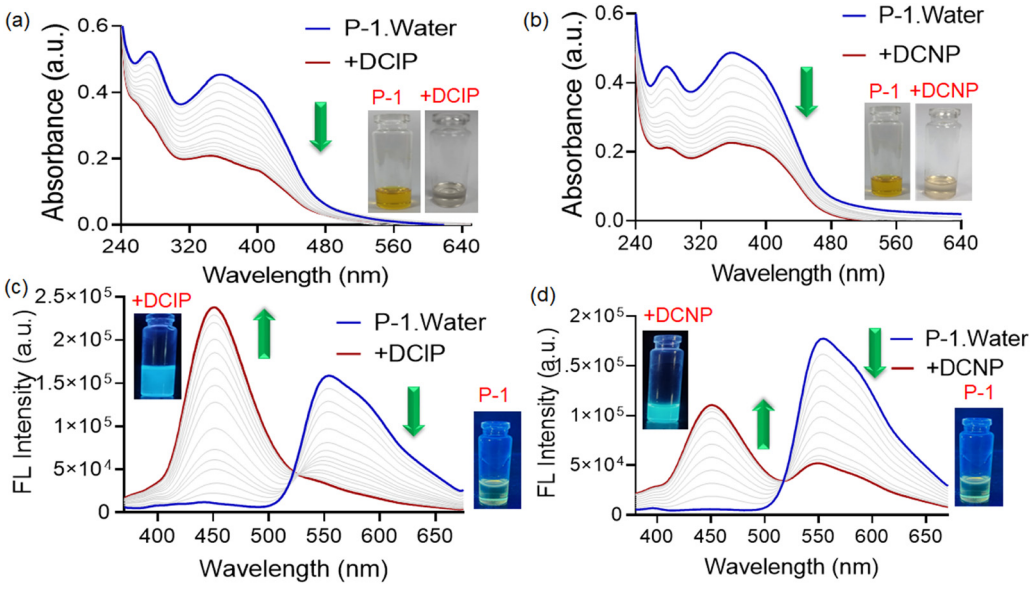

Fig. 5 (a) UV-visible titration of **P-1** (10 μM) with DClP (after incubation for 30 min) (0–160 μM) in an aqueous medium. (b) UV-visible titration of **P-1** (10 μM) with DCNP (after incubation for 30 min) (0–160 μM) in aqueous media. (c) Fluorescence titration of **P-1** (10 μM) with DClP (after incubation for 30 min) (0–160 μM) in an aqueous medium (λ_{ex} = 350 nm). (d) Fluorescence titration of **P-1** (10 μM) with DCNP (after incubation for 30 min) (0–160 μM) in an aqueous medium (λ_{ex} = 350 nm).

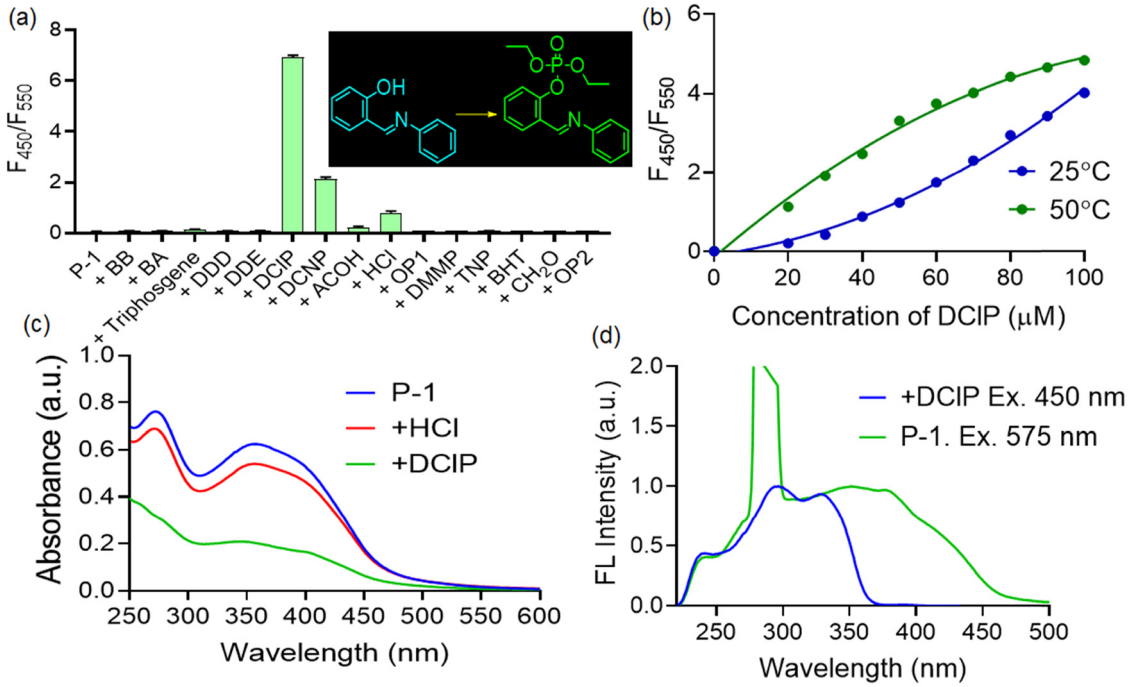

Fig. 6 (a) Change in fluorescence intensity of the compound **P-1** (10 μM) with different analytes (160 μM) in an aqueous medium (λ_{ex} = 350 nm) after incubation for 30 minutes. (b) Change in fluorescence intensity of the compound **P-1** upon addition of DCIP at different temperatures (25 °C and 50 °C) in an aqueous medium (λ_{ex} = 350 nm) after incubation for 30 minutes. (c) Absorption spectra of the compounds **P-1** (10 μM), **P-1@DCIP** (10 μM + 160 μM), and **P-1@HCl** (10 μM + 160 μM) in an aqueous medium after incubation for 30 minutes. (d) Excitation spectra of the compound **P-1** with and without the addition of DCIP in the aqueous medium after incubation for 30 minutes.

new characteristic peaks appeared at 2970 and 2924 cm^{-1}, and the –OH peak of **P-1** at 3053 cm^{-1} vanished, indicating phosphorylation of the –OH group.[50] Additionally, the imine bond peak has shifted from 1613 cm^{-1} to 1632 cm^{-1}, which may be due

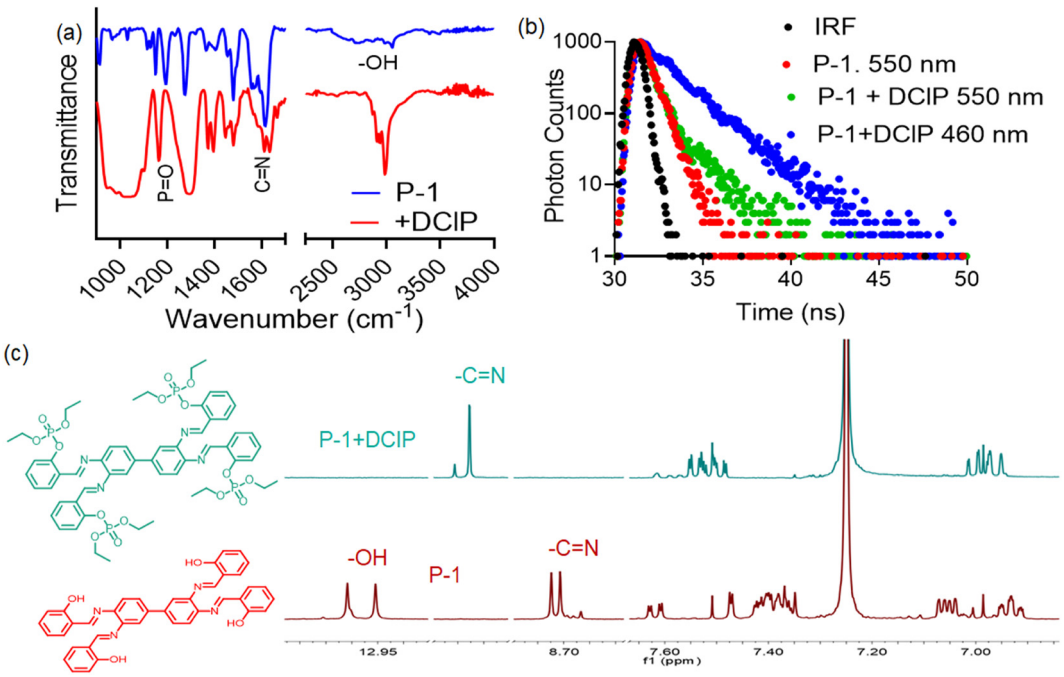

Fig. 7 (a) FTIR spectra of **P-1** (10 μM) compound with and without DCIP (160 μM) after incubation for 30 minutes. (b) Fluorescence lifetime of the compound **P-1** (10 μM) with and without DCIP (160 μM) after incubation for 30 minutes in an aqueous medium. (c) ^{1}H-NMR spectra of the compound **P-1** (5 mM) with and without the addition of DCIP (1 : 20) in the $CDCl_3$ medium after incubation for 30 min.

to the formation of intramolecular hydrogen bonding between the imine hydrogen and the oxygen center of the phosphate group. Again, DClP showed a characteristic peak at 1282 cm^{-1} for P═O stretching vibrations.[50] Upon interaction with **P-1**, the P═O stretching vibration was shifted to 1160 cm^{-1} which indicated the formation of a phosphorylated product.[51]

Furthermore, the sensing mechanism was investigated using the time-correlated single photon counting (TCSPC) technique. The fluorescence lifetime, a crucial parameter, remains unaffected by initial perturbation conditions like light source exposure time, fluorophore dispersion, and fluorescence intensity.[52] Upon the addition of DClP, the lifetime value of **P-1** increased from 150 ps to 430 ps (Fig. 7b). This enhancement can be attributed to the phosphorylation of the –OH group of **P-1**, which may destroy the J-aggregated structure and increase the enol emission, and as a consequence, photoluminescence is significantly enhanced.[53] The interaction of the compound **P-1** with DClP was also studied by ^{1}H and ^{31}P NMR analysis. In the ^{1}H NMR spectra, upon the addition of DClP the aromatic –OH proton of **P-1** (Fig. 7c) (denoted by '–OH') at δ = 13.2 ppm vanished, which may be due to the conversion of the –OH group into $–OPO(Et)_2$. On the other hand, the imine (–CH═N) proton located at ~8.7 ppm was shifted towards a higher chemical shift value (downfield shifted) due to the formation of a phosphorylated product which undergoes intermolecular hydrogen bonding with the imine proton. The electron density on the imine functional group proton moves towards the phosphorylation product that downfield shifted the –CH═N proton.[42,54] Again the ^{31}P-NMR spectra of DClP were compared with the NMR spectra of the **P-1**@DClP adduct (Fig. 8a). A shift in the δ value was observed from −1.5 ppm to +4.5 ppm upon the addition of compound **P-1** in the ^{31}P-NMR spectra of DClP. This indicates the phosphorylation of the –OH group and leaving of chlorine atom from the phosphate center of the DClP.[55]

To further understand the sensing mechanism, the mass spectra of compound **P-1** were recorded after the addition of DClP. In the mass spectra, the fragmented mass of the phosphorylated adduct of **P-1** was also observed (Fig. S9, ESI†). Upon the addition of DClP, the particle size of the **P-1@DClP** adduct increased to 400 ± 50 nm, showing an aggregated morphology which is also evident from the FESEM image of the adduct (Fig. 8c).

For a more feasible visualization of the change in fluorescence intensity of **P-1** upon the addition of DClP or DCNP, the data were represented in the form of CIE plots (Fig. 8b and d). The CIE chromaticity coordinates were found to be X = 0.4429 and Y = 0.5023 for **P-1** in the yellowish-green color region at room temperature. Upon the addition of DClP, the CIE chromaticity coordinates were found to be X = 0.1750, Y = 0.1426 in the blue colour region, and with DCNP, the CIE coordinates were found to be X = 0.2467, Y = 0.2431 in the greenish blue region. These data indicated that the change in fluorescence intensity is more pronounced in the case of DClP compared to DCNP.

Excitation–emission matrix (EEM) measurements were carried out upon the addition of different concentrations of DClP. In an EEM, the colours represent the intensity of fluorescence at different combinations of excitation and emission wavelengths.

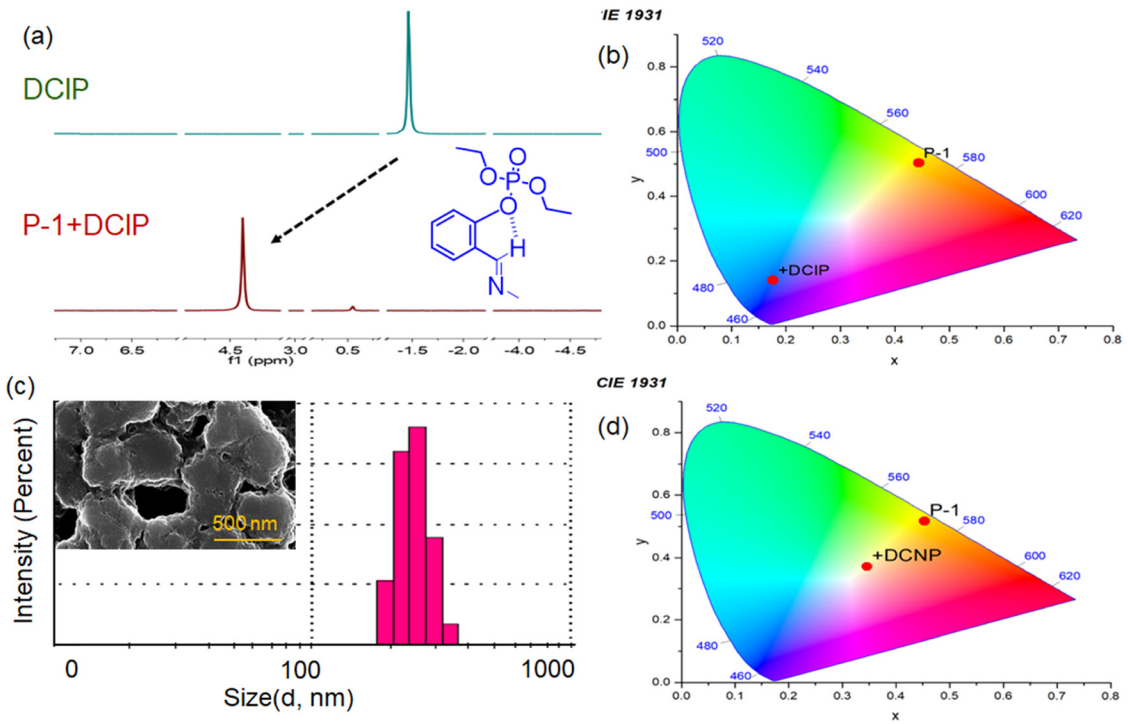

Fig. 8 (a) ^{31}P-NMR spectra of DClP and **P-1@DClP** in $CDCl_3$ medium after incubation for 30 min. (b) CIE plot of **P-1** (10 μM) compound with and without DClP after incubation for 30 min. (c) DLS and FESEM images (onset) of the **P-1@DClP** adduct. (d) CIE plot of **P-1** (10 μM) compound with and without DCNP after incubation for 30 min.

Red or orange indicates high fluorescence intensity, yellow or green indicates moderate to high fluorescence intensity, and cyan or blue indicates low to moderate fluorescence intensity.[56] The **P-1** compound showed higher fluorescence intensity at 560 nm when excited at 390 nm (shown in the red region) in the EEM plot (Fig. 9a). Initially, upon the addition of 25 μM DClP, the fluorescence intensity at 560 nm decreased and a distinct peak was observed at 450 nm (Fig. 9b). With an increase in the concentration from 25 μM to 160 μM, the peak at 560 nm disappeared, and a change was observed in the fluorescent profile of the lower region peak at 450 nm (Fig. 9c–f). These results aligned with the fluorescence titration results of **P-1** upon the addition of DClP, where the addition of DClP caused quenching of the emission maxima at 550 nm and enhancement in fluorescence intensity at 450 nm.

Finally, fluorescence titration was carried out by adding a saturated amount of DClP and DCNP to understand the kinetics of interaction between **P-1** and the analytes (Fig. 10a). In both cases, **P-1** showed a complete change in fluorescence intensity after ∼30 minutes. Additionally, the **P-1** compound showed a faster response to DClP compared to DCNP, indicating that a greater response to DClP may be due to the faster-leaving aptitude of chloride compared to cyanide.

3.5 Dimeric *vs.* monomeric salen-impact on analytical performance

We investigated the influence of binding units on DClP sensing by recording the fluorescence response upon interaction with two probes **P-1** and **P-2**. **P-1** has four binding sites, whereas **P-2** has two binding sites, and all the binding sites are susceptible to phosphorylation upon the addition of DClP. So, their extent of fluorogenic response was different towards DClP but not exactly proportional to the number of binding units present in the probe. Both the compounds showed a change in fluorescence intensity with the addition of DClP in the aqueous medium. As expected, the extent of change in fluorescence intensity was greater in the case of **P-1** (∼22-fold enhancement) at 450 nm compared to **P-2** (∼1.1-fold enhancement) at 440 nm (Fig. 10b and Fig. S10, ESI†). The significant difference in the fluorogenic response to DClP between the two probes indicates that it is not only dependent on the binding sites but also on the aggregation properties and the keto–enol equilibrium of the two probes. Based on the discussion of the photophysical properties of the probes, it is evident that probe **P-1** mainly exhibits enol emission, while probe **P-2** exhibits both enol and keto emission. The higher abundance of enol emission in **P-1** may be advantageous for the phosphorylation of the –OH group compared to **P-2**. Additionally, **P-1** exhibited significantly more aggregated emissions compared to **P-2**. Therefore, upon phosphorylation, the disaggregation of the aggregated structure will be more pronounced in the case of **P-1** compared to **P-2**.

3.6 Solvatochromic tuning of the sensing response

To understand the impact of solvent on DClP sensing by the **P-1** probe, fluorescence titration was carried out in DMSO (Fig. 10c). A change in the emission spectra was observed due

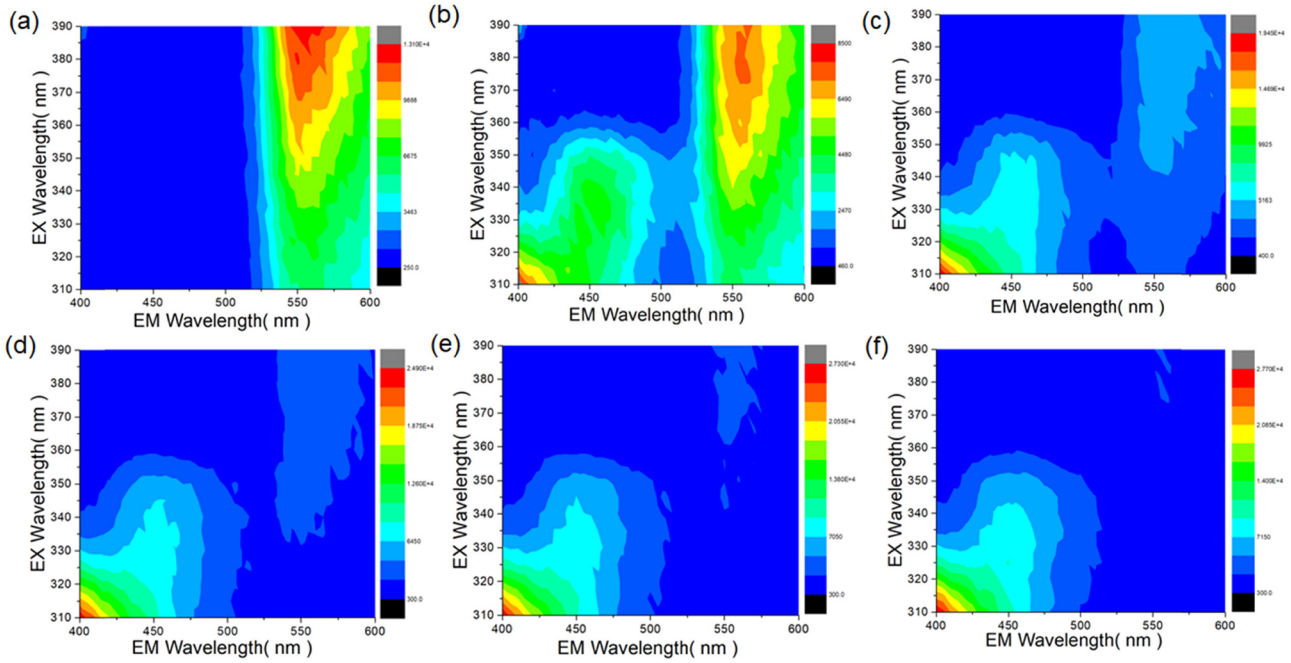

Fig. 9 (a) Excitation–emission matrix of **P-1** (10 μM) in an aqueous medium. (b) Excitation–emission matrix of **P-1** (10 μM) upon addition of DClP (25 μM) in an aqueous medium (after incubation for 30 min). (c) Excitation–emission matrix of **P-1** (10 μM) upon addition of DClP (50 μM) in an aqueous medium (after incubation for 30 min). (d) Excitation–emission matrix of **P-1** (10 μM) upon addition of DClP (75 μM) in an aqueous medium (after incubation for 30 min). (e) Excitation–emission matrix of **P-1** (10 μM) upon addition of DClP (100 μM) in an aqueous medium (after incubation for 30 min). (f) Excitation–emission matrix of **P-1** (10 μM) upon addition of DClP (160 μM) in an aqueous medium (after incubation for 30 min).

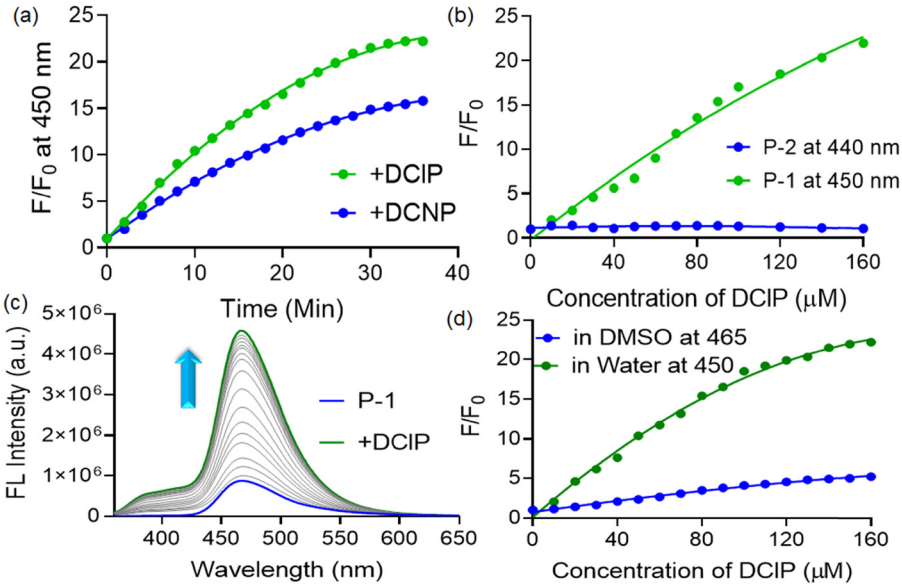

Fig. 10 (a) Kinetics plot of **P-1** (10 μM) compound upon addition of DClP and DCNP (0–160 μM) in an aqueous medium (λ_{ex} = 350 nm). (b) Change in fluorescence intensity of **P-1** (10 μM) and **P-2** (10 μM) upon addition of DClP (0–160 μM) in an aqueous medium (λ_{ex} = 350 nm). (c) Fluorescence titration of **P-1** (10 μM,) with DClP (0–160 μM) in DMSO medium (λ_{ex} = 350 nm). (d) Change in fluorescence intensity of **P-1** (10 μM) upon addition of DClP in aqueous and organic (DMSO) media (λ_{ex} = 350 nm).

to differences in the aggregation properties and the keto–enol equilibrium of the compound in different solvents. In DMSO, **P-1** showed a single emission maximum at 465 nm, indicative of prominent enol emission. In both water and DMSO, the fluorescence intensity increased upon the addition of DClP. However, the response differed between solvents. In water, a ratiometric change in fluorescence was observed, whereas in DMSO, only an enhancement in fluorescence intensity was observed. Specifically, the **P-1** compound exhibited a ~22.0-fold increase in fluorescence intensity at 450 nm in water upon the addition of DClP whereas in DMSO, the fluorescence intensity increased by ~5.2-fold at 465 nm (Fig. 10d). This difference is likely due to the several factors. Firstly, upon phosphorylation, the leaving aptitude of chlorine was favorable in a polar protic solvent (water) compared to a polar aprotic solvent (DMSO). Secondly, in water upon phosphorylation aggregated emission decreases due to inhibition of aggregation leading to a change in a more fluorogenic response which was not in the case of DMSO.[57,58] Lastly, the phosphorylated product was more stable in water compared to the organic medium as the phosphate groups are highly polar and can form multiple hydrogen bonds with water molecules.[59]

3.7 Mechanistic realization *via* computational studies

In this study, we performed energy minimization calculations for compounds **P-1** and **P-2**, as well as the phosphorylated adduct of **P-1**, using the Semiempirical level of theory method RPM6 with the ZDO basis set. The energy-optimized structure of compound **P-1** exhibited an optimized energy of +0.1028 a.u. and a dipole moment of 2.58 Debye whereas for compound **P-2**, the optimized energy and dipole moment were +0.067 a.u. and 3.8 Debye, respectively. In the optimized structure of **P-1**, the dihedral angle between the center and side rings (salicylidene unit) (which was labeled as A and B) was 179.8° and the dihedral angle between two phenyl rings on the center of the molecule (labelled as B and C) was 124.7° (Fig. 11a). For compound **P-2**, the dihedral angle between the center and adjacent phenyl rings (labelled as A and B) was 175.9° (Fig. S11, ESI†).

Frontier molecular orbital analysis revealed that the HOMO (highest occupied molecular orbital) of **P-1** was predominantly localized in the phenyl rings (A and B), with an energy of −0.302 a.u., situated at the center of the molecule on the phenyl ring (Fig. 11b). The LUMO (lowest unoccupied molecular orbital) orbitals were distributed over the adjacent salicylidene moieties, with an energy of −0.022 a.u. (Fig. 11c), whereas in **P-2**, the HOMO and LUMO were distributed over the whole molecule, with energies of −0.304 and −0.029 a.u., respectively (Fig. S12, ESI†).

To comment on the intramolecular charge distribution, we generated the electrostatic potential (ESP) map of the two compounds (**P-1** and **P-2**) using an iso-density value of 0.0004 a.u. Generally, in ESP maps, the red color indicates regions with an abundance of electrons (partial negative charge), while the blue color highlights areas with a deficit of electrons (partial positive charge). Light blue indicates slightly electron-deficient regions, yellow indicates slightly electron-rich domains, and green indicates neutral charge domains.[60] The ESP maps of **P-1** and **P-2** showed yellow and red colors, indicating that both molecules are overall electron-rich due to the presence of electronegative nitrogen and oxygen atoms, making them susceptible to electrophilic attack (Fig. S13 and S14, ESI†).

Upon phosphorylation of the –OH group (*i.e.*, the phosphorylated product of **P-1**), the optimized energy became −1.231 a.u., and the dipole moment increased to 5.43 Debye. In the phosphorylated adduct of **P-1**, the dihedral angle between the A (phosphorylated unit) and B moieties became 179.2°, and the dihedral angle between the B and C moieties

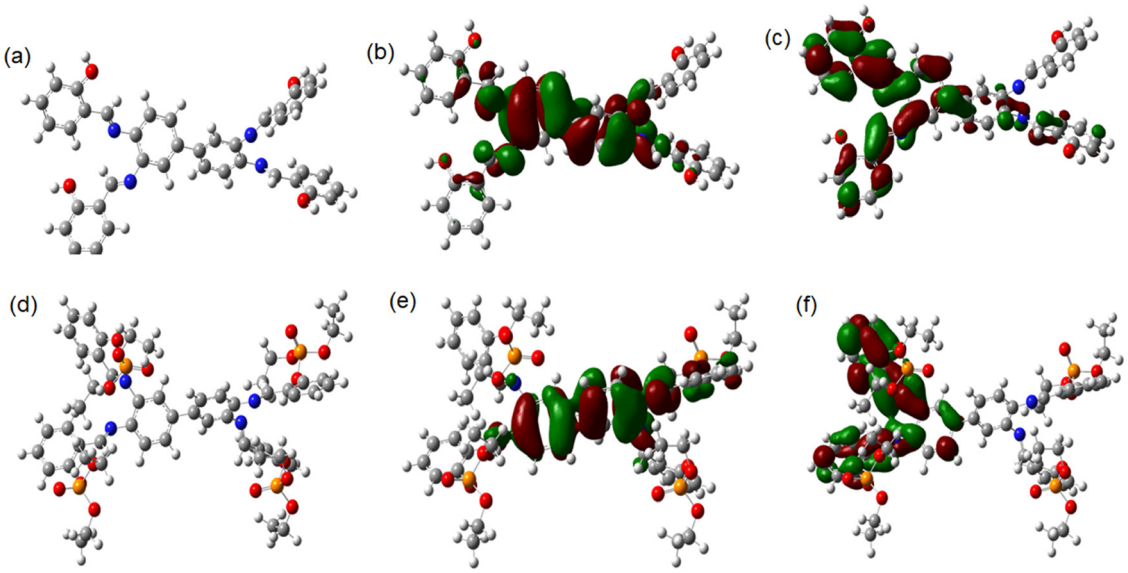

Fig. 11 (a) Optimized structure of the **P-1** compounds. (b) Highest occupied molecular orbital (HOMO) of **P-1**. (c) Lowest unoccupied molecular orbital (LUMO) of **P-1**. (d) Optimized structure of the phosphorylated adduct of **P-1**. (e) Highest occupied molecular orbital (HOMO) of the phosphorylated adduct of **P-1**. (f) Lowest unoccupied molecular orbital (LUMO) of the phosphorylated adduct of **P-1**.

was 130.6° (Fig. 11d). The HOMO and LUMO energies of the phosphorylated adduct were −0.303 and −0.027 a.u., respectively (Fig. 11e and f). In the ESP map of the phosphorylated adduct of **P-1**, the red region was mainly distributed at the center of the whole molecule and was not observed at the oxygen atom as in **P-1** (Fig. S15, ESI†). This indicated that upon phosphorylation, the electrophilic character of the oxygen atom decreases.

Furthermore, Mulliken charge distribution plots were obtained to understand the change in charge density intensity in the salicylidene ring before and after phosphorylation (Fig. S16 and S17, ESI†). Before phosphorylation, the overall Mulliken charge on the salicylidene ring (including the –OH group) was +0.015 a.u., and after phosphorylation (including –OPO(OEt)2), it was slightly higher at +0.017 a.u. This indicated that due to phosphorylation, the overall positive charge on the ring increases, thereby decreasing the electrophilic character of the ring.

3.8 Paper strips and detection of nerve gases in the vapour phase

Apart from the liquid phase, the sensing of DClP was also important in the vapor phase as it was used as a gaseous weapon in warfare.[61] Due to this, paper strips can be useful techniques over conventional experimental procedures as the high costs associated with instrumental techniques are significant drawbacks to the practical utility of chemo-sensors.[62–67] To assess the practical usefulness of our probe **P-1** for on-site detection of DClP nerve gas mimics, we conducted experiments using Whatman-41 filter paper strips. Small, equally sized filter papers were immersed in a 3 mM DMSO solution of **P-1** for several hours and then dried in a hot air oven at 60 °C. The papers turned yellow, and the intensity of the yellow color was analyzed using Image-J software at different time intervals to assess the stability of the paper strips under ambient conditions (Fig. 12a). However, upon exposure to DClP vapor (0–150 μM) for 10 minutes the paper strips changed from deep yellow to light yellow. Under UV light, the **P-1**-doped paper strips exhibited blue-green fluorescence and when exposed to DClP vapour showed cyan fluorescence. This whole experiment was carried out following the dip-stick method reported in previous literature.[15] Initially, a sample-coated paper strip was attached to the glass vial. Under the glass vial, different amounts of DClP liquid were taken, and the glass vial was sealed and kept for 10 minutes for the DClP vapor to come into contact with the paper strip (Fig. S18, ESI†). The fluorescence intensity of the paper strip was measured under the UV light of a 365 nm laser before and after the exposure to DClP vapor. The intensity of cyan fluorescence increases with higher concentrations. These changes in the intensity of the cyan color were measured using image-J software (Fig. 12b).

3.9 Detection of nerve gases in the real life sample

Soil contamination by chemical warfare agents (CWAs) poses serious risks to both civilian and military populations, potentially causing severe health problems or fatalities. Again, the contamination of soil with CWAs, their precursors, or degradation products is often associated with military or terrorist activities, whether related to storage, production, disposal, or deployment. Consequently, detecting DClP in soil samples is essential for managing and mitigating these hazards.[68] Again, the probe **P-1** was also employed for the detection of DClP in soil samples. To detect DClP in soil samples initially, two samples (marked as S-1 and S-2) were collected from the university campus and then thoroughly ground using a motor and pestle. After that, the powder soil sample (1g) was dissolved in 100 ml water and filtered using the Whatmann-1 filter paper to remove any undissolved impurities. Then this soil solution was spiked with DClP at different concentrations. The background spectra of **P-1** were

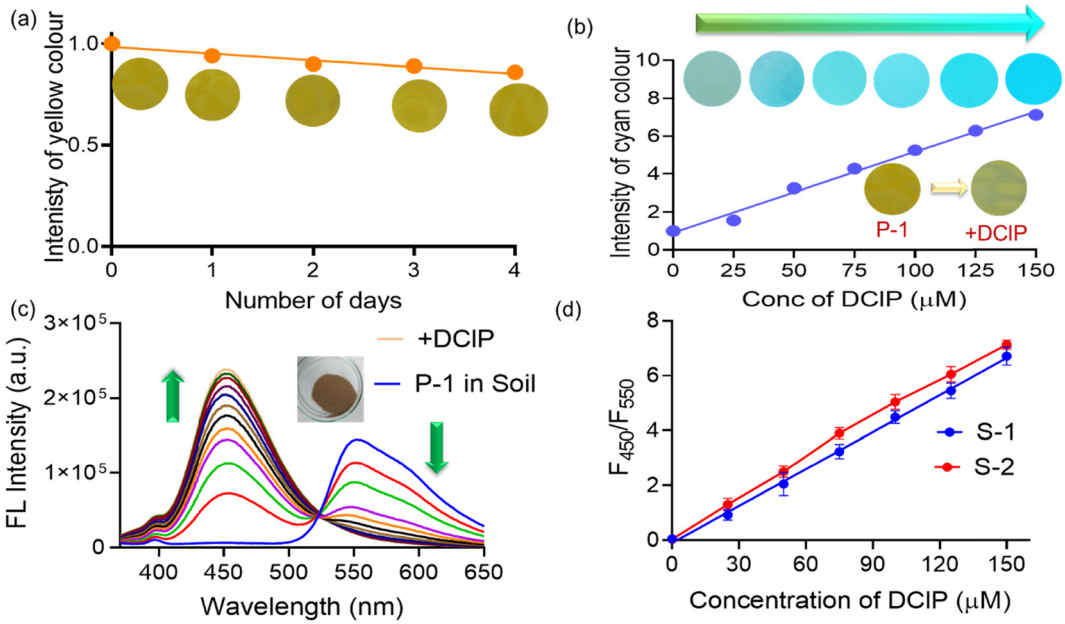

Fig. 12 (a) The intensity of the yellow color of the **P-1** coated paper strips was analyzed by Image J software against time. (b) Change in the cyan color of the **P-1** coated paper strip upon addition of DClP under UV light and analyzed by image J software. (c) Fluorescence spectra of **P-1** (10 μM) in soil solution and response with a spiking sample of DClP (150 μM) (λ_{ex} = 350 nm). (d) Ratiometric change in fluorescent intensity of **P-1** with the different concentration of DClP spiked soil samples (S-1 and S-2) (λ_{ex} = 350 nm).

recorded in only soil solution and not much interference was found and then spiked soil solution was measured by the change in fluorescence intensity (Fig. 12c and d). The limits of detection for DClP were 15.2 ppb and 14.8 ppb with recovery values ranging between 95.4–97.8%. The relative standard deviation (RSD) was within 2–3%, indicating the practicality and reliability of the proposed probe.

4. Conclusion

In this study, we have developed and produced two fluorescent ESIPT active salen derivatives (**P-1** and **P-2**) for detecting toxic nerve gas mimics of DClP in both aqueous and organic media. Initially, we explored the difference in the photophysical and aggregation properties of these derivatives. In an aqueous medium, both the probes showed change in fluorescence upon the addition of DClP and the extent of change was greater in the case of **P-1** (∼22.0-fold) compared to **P-2** (∼1.0-fold) due to its dimeric structure which changes its aggregation behavior and keto–enol equilibrium in water. The **P-1** compound exhibited a ratiometric fluorescence change of approximately 7.0-fold in response to DClP in an aqueous medium. Different spectroscopic investigations were carried out such as NMR, FTIR, FESEM, UV-vis, lifetime, and fluorescence to understand the mechanism of sensing. The mechanistic investigation suggested that the phosphorylation of the hydroxy group led to changes in the keto–enol equilibrium and aggregation state of compound **P-1**. Furthermore, an elaborate investigation was carried out to understand the effect of solvents (organic and aqueous), temperature, and time of interaction between the probe and analyte. The compound **P-1** exhibited a change in the ratiometric response to DClP in an aqueous medium while showing only turn-on sensing in DMSO. In DMSO, the **P-1** compound exhibited a ∼22.0-fold increase in fluorescence intensity at 450 nm in water upon the addition of DClP whereas in DMSO, the fluorescence intensity increased by ∼5.2-fold at 465 nm. This may be attributed to the alteration in the keto–enol equilibrium and the extent of aggregation of **P-1** in the two solvents as well as the stability of the phosphorylated product. The minimum detectable limit for DClP by **P-1** was found to be as low as ∼5.0 ppb. The interaction time between DClP and **P-1** was approximately 30 minutes, so each sample was incubated for 30 minutes before measurement. Theoretical calculations were carried out to validate the experimental findings. Then this probe was employed to detect the nerve gas mimics DClP in the spiked soil sample. The limit of detection of DClP in soil samples was found in the range of 14.8–15.2 ppb, with recovery values ranging from 95.4% to 97.8%. The relative standard deviation (RSD) was within 2–3%, demonstrating the practicality and reliability of the proposed probe. Finally, sample-coated paper strips were prepared for easy on-site detection of nerve gases in the vapor phase, and the color change was analyzed using image-J software.

Data availability

The author will provide the data on reasonable request.

Conflicts of interest

The author herewith declares no conflict of interest for the manuscript, entitled, Comparative analysis of monomeric *vs.*

dimeric salen fluorescent probes: transition from a turn-on to ratiometric response towards nerve gas agents in organic to aqueous media submitted to Materials Advances journal.

Acknowledgements

N. D. and S. M. thank the SERB-SRG grant (SRG/2022/000031) and ICMR-ITR grant (2021-8350) for financial support and a research fellowship. The authors also thank the central analytical facilities of BITS-Pilani for providing technical support and laboratory facilities.

References

1 G. Zappalà, E. Dumont, G. Soufi, N. Molander, A. Abbaspourmani, D. Asoli and A. Boisen, Evaluation of the SERS performances of Tabun and VX label-free detection in complex and multicomponent fluids, *Heliyon*, 2024, DOI: 10.1016/j.heliyon.2024.e32181.
2 K. Ganesan, S. K. Raza and R. Vijayaraghavan, Chemical warfare agents, *J. Pharm. BioAllied Sci.*, 2010, **2**, 166–178.
3 S. W. Wiener and R. S. Hoffman, Nerve agents: a comprehensive review, *J. Intensive Care Med.*, 2004, **19**, 22–37.
4 S. Costanzi, J. H. Machado and M. Mitchell, Nerve agents: what they are, how they work, how to counter them, *ACS Chem. Neurosci.*, 2018, **9**, 873–885.
5 S. Mondal, B. Krishna, S. Roy and N. Dey, Discerning toxic nerve gas agents via a distinguishable 'turn-on' fluorescence response: multi-stimuli responsive quinoline derivatives in action, *Analyst*, 2024, **149**, 3097–3107.
6 N. Dey, S. Jha and S. Bhattacharya, Visual detection of a nerve agent simulant using chemically modified paper strips and dye-assembled inorganic nanocomposite, *Analyst*, 2018, **143**, 528–535.
7 S. Royo, A. M. Costero, M. Parra, S. Gil, R. Martínez-Mañez and F. Sancenón, Chromogenic, specific detection of the nerve-agent mimic DCNP (a Tabun mimic), *Chem. – Eur. J.*, 2011, **25**, 6931–6934.
8 K. Kim, O. G. Tsay, D. A. Atwood and D. G. Churchill, Destruction and detection of chemical warfare agents, *Chem. Rev.*, 2011, **111**, 5345–5403.
9 J. Jaworska, H. Van Genderen-Takken, A. Hanstveit, E. van de Plassche and T. Feijtel, Environmental risk assessment of phosphonates, used in domestic laundry and cleaning agents in the Netherlands, *Chemosphere*, 2002, **47**, 655–665.
10 P. Rearden and P. B. Harrington, Rapid screening of precursor and degradation products of chemical warfare agents in soil by solid-phase microextraction ion mobility spectrometry (SPME–IMS), *Anal. Chim. Acta*, 2005, **545**, 13–20.
11 A. J. Russell, J. A. Berberich, G. F. Drevon and R. R. Koepsel, Biomaterials for mediation of chemical and biological warfare agents, *Annu. Rev. Biomed. Eng.*, 2003, **5**, 1–27.
12 M. Wheelis, Biotechnology and chemical weapons control, *Pure Appl. Chem.*, 2002, **74**, 2247–2251.
13 H. Sohn, S. Létant, M. J. Sailor and W. C. Trogler, Detection of fluorophosphonate chemical warfare agents by catalytic hydrolysis with a porous silicon interferometer, *J. Am. Chem. Soc.*, 2000, **122**, 5399–5400.
14 Y. Lin, F. Lu and J. Wang, Disposable carbon nanotube modified screen-printed biosensor for amperometric detection of organophosphorus pesticides and nerve agents, *Electroanalysis*, 2004, **16**, 145–149.
15 Z. Rahman, N. Tohora, M. Mahato, S. Ahamed, T. Sultana and S. K. Das, Fluorogenic, specific detection of sarin gas mimic, diethylchlorophosphate, *J. Photochem. Photobiol., A*, 2023, **444**, 115007.
16 F. W. Dagnaw, Y. P. Cai and Q. H. Song, Rapid and sensitive detection of nerve agent mimics by meso-substituted BODIPY piperazines as fluorescent chemosensors, *Dyes Pigm.*, 2021, **189**, 109257.
17 Q. Chen, J. Liu, S. Liu, J. Zhang, L. He, R. Liu and K. Zhang, Visual and rapid detection of nerve agent mimics in gas and solution phase by a simple fluorescent probe, *Anal. Chem.*, 2023, **95**, 4390–4394.
18 L. Zeng, H. Zeng, L. Jiang, S. Wang, J. T. Hou and J. Yoon, A single fluorescent chemosensor for simultaneous discriminative detection of gaseous phosgene and a nerve agent mimic, *Anal. Chem.*, 2019, **91**, 12070–12076.
19 N. Klinhom, N. Saengsuwan, S. Sriyab, P. Prompinit, S. Hannongbua and S. Suramitr, Photophysical properties for excited-state intramolecular proton transfer (ESIPT) reaction of *N*-salicylidene-*o*-aminophenol: Experimental and DFT based approaches, *Spectrochim. Acta, Part A*, 2019, **206**, 359–366.
20 M. Joshi and A. R. Choudhury, *Salen Type Ligand as a Selective and Sensitive Nickel(II) ion Chemosensor: A Combined Investigation with Experimental and Theoretical Modelling*, 2018.
21 J. Chi, Y. Song and L. Feng, A ratiometric fluorescent paper sensor based on dye-embedded MOF for high-sensitive detection of arginine, *Biosens. Bioelectron.*, 2023, **241**, 115666.
22 S. Mondal and N. Dey, Modulating Fluorescent Responses in Organic-Doped Polyethylenimine Composites: Impact on Pyrophosphate Detection and Biogenic Phosphate Analysis, *ACS Appl. Polym. Mater.*, 2024, **6**, 10242–10253.
23 N. Kumari, N. Dey, S. Jha and S. Bhattacharya, Ratiometric, reversible, and parts per billion level detection of multiple toxic transition metal ions using a single probe in micellar media, *ACS Appl. Mater. Interfaces*, 2013, **5**, 2438–2445.
24 A. Pal and N. Dey, A chromogenic anthraimidazoldione probe for ratiometric analysis of Hg^{2+} exclusively at mesoscopic interface: Screening of real-life biological samples, *Colloids Surf., A*, 2024, **687**, 133397.
25 S. Mondal and N. Dey, Polyethyleneimine-derived fluorescent conjugate for trace-level detection of multiple ions via signal amplification, *J. Photochem. Photobiol., A*, 2024, **455**, 115686.
26 A. Gulyani, N. Dey and S. Bhattacharya, A unique self-assembly-driven probe for sensing a lipid bilayer:

ratiometric probing of vesicle to micelle transition, *Chem. Commun.*, 2018, **54**, 5122–5125.
27 V. R. Singh and P. K. Singh, A supramolecule based fluorescence turn-on and ratiometric sensor for ATP in aqueous solution, *J. Mater. Chem. B*, 2020, **8**, 1182–1190.
28 Y. Wang, M. Zhu, E. Jiang, R. Hua, R. Na and Q. X. Li, A simple and rapid turn on ESIPT fluorescent probe for colorimetric and ratiometric detection of biothiols in living cells, *Sci. Rep.*, 2017, **7**, 4377.
29 T. Mutai, H. Tomoda, T. Ohkawa, Y. Yabe and K. Araki, Switching of polymorph-dependent ESIPT luminescence of an imidazo[1,2-a]pyridine derivative, *Angew. Chem.*, 2008, **120**, 9664–9666.
30 N. Basaric, N. Došlić, J. Ivkovic, Y. H. Wang, J. Veljkovic, K. Mlinaric-Majerski and P. Wan, Excited state intramolecular proton transfer (ESIPT) from phenol to carbon in selected phenylnaphthols and naphthylphenols, *J. Org. Chem.*, 2013, **78**, 1811–1823.
31 M. E. Belowich and J. F. Stoddart, Dynamic imine chemistry, *Chem. Soc. Rev.*, 2012, **41**, 2003–2024.
32 R. Chen, Q. Li, Z. Zhang, K. Xu, L. Sun, J. Ma and H. Wu, Solvent effect on ESIPT process of N-(8-Quinolyl) salicylaldimine: A DFT/TD-DFT calculation, *J. Photochem. Photobiol., A*, 2023, **436**, 114335.
33 S. Sharma, A. Dhir and C. P. Pradeep, ESIPT induced AIEE active material for recognition of 2-thiobarbituric acid, *Sens. Actuators, B*, 2014, **191**, 445–449.
34 S. Ravi, P. Priyadharshini, G. Deviga, M. Mariappan, S. Karthikeyan, M. Pannipara and S. P. Anthony, Water sensitive fluorescence tuning of V-shaped ESIPT fluorophores: Substituent effect and trace amount water sensing in DMSO, *Spectrochim. Acta, Part A*, 2024, **309**, 123838.
35 S. Gadiyaram, V. D. Ghule, A. Ghosh and D. A. Jose, An ESIPT-based fluorescent probe for the detection of multiple analytes and a facile approach to discriminate between arsenate and pyrophosphate in water, *Sens. Diagn.*, 2022, **1**, 1224–1235.
36 S. K. Panja, Dipolar state assisted aggregation induced optical behavior of push-pull Salen-type Schiff base (BIHyDE) in solution, *J. Mol. Struct.*, 2021, **1234**, 130140.
37 L. Liu, J. Hao, Y. Shi, J. Qiu and C. Hao, Roles of hydrogen bonds and π–π stacking in the optical detection of nitroexplosives with a luminescent metal–organic framework as the sensor, *RSC Adv.*, 2015, **5**, 3045–3053.
38 S. S. Zadeh, A. Ebrahimi and A. Shahraki, The impact of π–π stacking interactions on photo-physical properties of hydroxyanthraquinones, *Spectrochim. Acta, Part A*, 2023, **292**, 122453.
39 S. K. Panja, J-type aggregation and thermochromic behavior of a Schiff base in solution: Role of keto–enol tautomerization, *Spectrochim. Acta, Part A*, 2020, **229**, 117860.
40 H. Piwoński, S. Nozue, H. Fujita, T. Michinobu and S. Habuchi, Organic J-aggregate nanodots with enhanced light absorption and near-unity fluorescence quantum yield, *Nano Lett.*, 2021, **21**, 2840–2847.
41 Y. Hong, J. W. Lam and B. Z. Tang, Aggregation-induced emission, *Chem. Soc. Rev.*, 2011, **40**, 5361–5388.
42 S. Kundu, S. Saha and P. Sahoo, Rapid and selective visual detection of DCNP (nerve gas mimic) in sea water and soil with a simple paper strip, *Results Chem.*, 2019, **1**, 100014.
43 X. S. Yu, M. M. Zhu, R. Zuo, Y. Peng and Y. W. Wang, A Turn-On and Colorimetric Probe Based on Isophorone Skeleton for Detecting Nerve Agent Mimic Diethyl Chlorophosphite, *Molecules*, 2023, **28**, 3237.
44 C. T. Cao, L. Li, C. Cao and J. Liu, The effect of intramolecular hydrogen bond on the ultraviolet absorption of bi-aryl Schiff bases, *J. Phys. Org. Chem.*, 2021, **34**, e4164.
45 G. Dhaka, N. Kaur and J. Singh, Exploiting the INHIBIT-ESIPT mechanism for the design of fluorescent chemosensor with a large blue-shift in emission, *J. Photochem. Photobiol., A*, 2017, **335**, 174–181.
46 N. Kumari, M. Jassal and A. K. Agrawal, A facile method for the phosphorylation of cellulosic fabric via atmospheric pressure plasma, *Carbohydr. Polym.*, 2021, **256**, 117531.
47 R. Passier, J. P. Ritchie, C. Toro, C. Diaz, A. E. Masunov, K. D. Belfield and F. E. Hernandez, Thermally controlled preferential molecular aggregation state in a thiacarbocyanine dye, *J. Chem. Phys.*, 2010, **133**, 134508.
48 A. P. Deshmukh, N. Geue, N. C. Bradbury, T. L. Atallah, C. Chuang, M. Pengshung and J. R. Caram, Bridging the gap between H-and J-aggregates: Classification and supramolecular tunability for excitonic band structures in two-dimensional molecular aggregates, *Chem. Phys. Rev.*, 2022, **3**, 021401.
49 H. Gu, W. Wang, W. Wu, M. Wang, Y. Liu, Y. Jiao and X. Chen, Excited-state intramolecular proton transfer (ESIPT)-based fluorescent probes for biomarker detection: design, mechanism, and application, *Chem. Commun.*, 2023, **59**, 2056–2071.
50 Y. Liu, L. Zhou, F. Ding, S. Li, R. Li, Z. Li and X. Ren, Flame-retardant cotton fabrics modified with phosphoramidate derivative via electron beam irradiation process, *J. Ind. Text.*, 2021, **51**, 396–408.
51 G. Keglevich, R. E. Puskás, A. Grün and I. Csontos, Monitoring the Phosphorylation of Phenol with Diethyl Chlorophosphate in Aqueous Medium in the Presence of Sodium Hydroxide by in Situ Fourier Transform Infrared Spectroscopy, *Phosphorus, Sulfur Silicon*, 2010, **185**, 832–837.
52 J. Chen, Z. Liu, X. Li, P. Liu, J. Jiang and X. Nie, Thermal behavior of epoxidized cardanol diethyl phosphate as novel renewable plasticizer for poly(vinyl chloride), *Polym. Degrad. Stab.*, 2016, **126**, 58–64.
53 R. Datta, T. M. Heaster, J. T. Sharick, A. A. Gillette and M. C. Skala, Fluorescence lifetime imaging microscopy: fundamentals and advances in instrumentation, analysis, and applications, *J. Biomed. Opt.*, 2020, **25**, 071203.
54 T. Sultana, M. Mahato, N. Tohora, S. Ahamed, P. Pramanik, S. Ghanta and S. K. Das, A phthalimide-based turn on fluorosensor for selective and rapid detection of G-series nerve agent's mimics, *J. Photochem. Photobiol., A*, 2023, **439**, 114584.
55 Y. J. Jang, D. P. Murale and D. G. Churchill, Novel reversible and selective nerve agent simulant detection in conjunction

with superoxide ''turn-on'' probing, *Analyst*, 2014, **139**, 1614–1617.

56 C. A. Stedmon and R. Bro, Characterizing dissolved organic matter fluorescence with parallel factor analysis: a tutorial, *Limnol. Oceanogr.: Methods*, 2008, **6**, 572–579.

57 X. Xu, X. Liu, Z. Nie, Y. Pan, M. Guo and S. Yao, Label-free fluorescent detection of protein kinase activity based on the aggregation behavior of unmodified quantum dots, *Anal. Chem.*, 2011, **83**, 52–59.

58 M. Lin, J. Huang, F. Zeng and S. Wu, A fluorescent probe with aggregation-induced emission for detecting alkaline phosphatase and cell imaging, *Chem. – Asian J.*, 2019, **14**, 802–808.

59 K. Karathanou and A. N. Bondar, Dynamic water hydrogen-bond networks at the interface of a lipid membrane containing palmitoyl-oleoyl phosphatidylglycerol, *J. Membr. Biol.*, 2018, **251**, 461–473.

60 R. Arulraj, S. Sivakumar, S. Suresh and K. Anitha, Synthesis, vibrational spectra, DFT calculations, Hirshfeld surface analysis and molecular docking study of 3-chloro-3-methyl-2, 6-diphenylpiperidin-4-one, *Spectrochim. Acta, Part A*, 2020, **232**, 118166.

61 G. J. Fitzgerald, Chemical warfare and medical response during World War I, *Am. J. Public Health*, 2008, **98**, 611–625.

62 S. Mondal and N. Dey, Flexible metallosalen complex for pyrophosphate sensing in biological milieu: Use disassembly strategy for signal amplification, *J. Mol. Liq.*, 2024, **398**, 123914.

63 S. Mondal, M. Karar and N. Dey, Dye-surfactant co-assembly as the chromogenic indicator for nanomolar level detection of Cu(I) ions via a color-changing response, *J. Mater. Chem. B*, 2023, **11**, 4111–4120.

64 H. V. Barkale and N. Dey, Functionalized Cyanostilbene-based Nano-AIEgens: Multipoint Binding Interactions for Improved Sensing of Gallic Acid in Real-Life Food Samples, *J. Mater. Chem. B*, 2024, **12**, 8746–8756.

65 A. Pal, M. Karar and N. Dey, Visualizing anions by color changing response: Exploitation of pyrimidine-based probe for simultaneous detection of CN^- and F^- ions, *J. Mol. Struct.*, 2024, **1307**, 137836.

66 A. Pal, O. Sarkar, N. R. Pramanik and N. Dey, Design of ESIPT-Based Fluorescent Probes for Dual-Mode Sensing of Cyanide: Application to Rapid On-Location Detection and Screening of Natural Water Samples, *Ind. Eng. Chem. Res.*, 2024, **63**(19), 8489–8496.

67 B. Chettri, A. Pal, S. Jha and N. Dey, Tuning Sensing Efficacy of Anthraimidazoledione-Based Charge Transfer Dyes: Nitro Group Positioning Impact, *Dalton Trans.*, 2024, **53**(14), 6343–6351.

68 P. Rearden and P. B. Harrington, Rapid Screening of Precursor and Degradation Products of Chemical Warfare Agents in Soil by Solid-Phase Microextraction Ion Mobility Spectrometry (SPME–IMS), *Anal. Chim. Acta*, 2005, **545**(1), 13–20.